



# Weather radar and ancillary observations of the convective system causing the northern Persian Gulf meteotsunami on 19 March 2017

Mohammad Hossein Kazeminezhad, et al. *[full author details at the end of the article]*

Received: 21 April 2020 / Accepted: 25 July 2020 / Published online: 8 August 2020  
© Springer Nature B.V. 2020

## Abstract

This study documents the atmospheric system driving the observed meteotsunami waves that hit the northern Persian Gulf on 19 March 2017 during high tide. This destructive meteotsunami event resulted in coastal inundations that reached several hundred metres inland along the 100-km coastline between the cities of Dayyer and Asaluyeh and caused the death or injury of 27 persons. Based on previously published research, eyewitness reports, oceanic and atmospheric observations, including synoptic station and weather radar data, and available reanalysis ERA5 products, this study provides new insights into destructive events, particularly mesoscale atmospheric systems conjoined with observed meteotsunami waves. Precipitation intensity, maximum reflectivity and echo top height images provided by the weather radar covering the affected area and the area over which the meteotsunamigenic disturbance travelled revealed that a strong convective system that encompassed the mid- and upper troposphere entered the northern Persian Gulf approximately 4 h before the event and moved eastward. Two hours before reaching the affected coastline, this convective system was reshaped to an elongated and narrow squall line varying between 70 and 130 km in length with a width of less than 10 km and travelled at an average speed of approximately 24 m/s over the sea. The peak maximum reflectivity of the squall line always surpassed 40 dBZ, while it increased to 60 dBZ near the Dayyer area. As such, intense atmospheric disturbances are known to be associated with sharp air pressure increases, and these disturbances were found to resonantly pump energy to the ocean through Proudman resonance for over 12 or more disturbance wavelengths (i.e. up to 120 km in this study). A half-metre meteotsunami wave was presumably created in the open sea and then amplified while travelling towards the shore where it broke as a meteotsunami bore and inundated the coastal areas. Further research on the physical mechanisms driving the interactions between meteotsunamigenic disturbances and ocean responses, the recurrence of such events and meteotsunami hazard assessments along the affected coastline is envisaged.

**Keywords** Meteotsunami · Weather radar · Mesoscale atmospheric system · Squall line · Proudman resonance · Northern Persian Gulf

## 1 Introduction

Throughout the world, proximity to the sea is perceived as an exceptional economic advantage; however, marine hazards affecting coastal areas pose a serious threat to local communities' way of life. Sudden sea level rise, originating from either geological (e.g. tsunami) or meteorological (e.g. storm surge) conditions and resulting in inundations that can penetrate several kilometres inland, is one of the most destructive processes affecting low-lying coastlines (Mafi-Gholami et al. 2019). In particular, meteorological tsunamis or meteotsunamis are observed worldwide in oceans and coastal seas (Monserrat et al. 2006; Pattiaratchi and Wijeratne 2015; Vilibić et al. 2016). These phenomena resemble long ocean waves that may be amplified to several metres in either open coastal regions or harbours and bays and are generated by atmospheric disturbances. In the past, several metre-high meteotsunami waves were observed along open sea beaches (referred to as “beach meteotsunamis”, Rabinovich 2020) such as the Dayyer region, along the shores of Florida (Churchill et al. 1995; Sallanger et al. 1995), the U.S. East Coast (Lipa et al. 2014; Vilibić et al. 2014), the Great Lakes (Ewing et al. 1954; Linares et al. 2019), the Brazilian and Argentinian coasts (Dragani et al. 2014) and the north-western Black Sea coast (Vilibić et al. 2010; Šepić et al. 2018b). These waves sometimes result in deaths or injuries and substantial damage to coastal infrastructures (Hibiya and Kajiura 1982; Vučetić et al. 2009; Pattiaratchi and Wijeratne 2015).

The crucial condition for amplifying meteotsunami waves to destructive levels is the existence of an efficient mechanism for the resonant transfer of energy between the atmosphere and the ocean, and the most commonly documented mechanisms are the Proudman resonance (Proudman 1929) and the Greenspan resonance (Greenspan 1956). These resonances are the most efficient when the speed of the atmospheric meteotsunamigenic forcing is equal to the speed of long ocean or edge waves over several wavelengths of atmospheric disturbance (Hibiya and Kajiura 1982; Vilibić 2008; Šepić et al. 2015a), while they are potentially further amplified by coastal shallowing and other topographic changes (Venell 2010; Williams et al. 2020). The drivers of these meteotsunamigenic disturbances may be of different atmospheric origins: (1) wave-ducting, which has been largely researched in the Mediterranean, a known meteotsunami hot spot (Monserrat and Thorpe 1996); (2) squall lines (Churchill et al. 1995; Paxton and Sobien 1998); (3) wave-CISK (convective instability of the second kind, Belušić et al. 2007); (4) fast moving storms such as derechos (Šepić and Rabinovich 2014; Bechle et al. 2016); (5) convective cells (Sibley et al. 2016; Williams et al. 2019); (6) tropical cyclones and hurricanes (Shi et al. 2020) and others. However, all of these atmospheric processes are highly mesoscale and require non-standard meteorological measurements at a high resolution, which are rarely available from regular meteorological networks. To document the spatial and temporal changes at the mesoscale, including the estimation of the basic meteotsunamigenic disturbance parameters (intensity, horizontal gradients, disturbance speed and propagation direction), weather radar observations were found to be quite useful in meteotsunami research (Vilibić et al. 2014; Wertman et al. 2015; Sibley et al. 2016; Linares et al. 2019; Shi et al. 2020).

However, the Persian Gulf, which is a shallow (rarely deeper than approximately 90 m) and elongated (ca. 990 km by 200 km) semi-enclosed sea separated from the oceans by the 56 km wide Strait of Hormuz (Fig. 1), is not known to be exceptionally sensitive to extreme sea level hazards and meteotsunamis. Indeed, under normal conditions, the Persian Gulf is characterized by (1) tides ranging from 1 to 2 metres (Akbari et al. 2016; Soltanpour et al. 2018), (2) storms generally not associated with coastal flooding, as mostly connected to

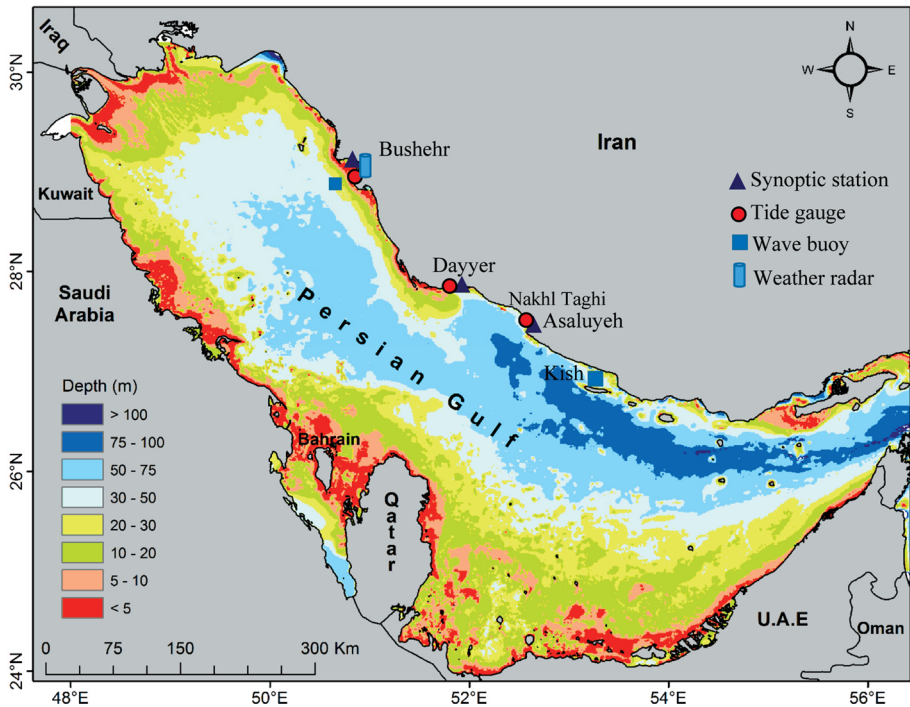


**Fig. 1** Map of the Persian Gulf and locations of the cities of Bushehr, Dayyer, Asaluyeh and Nakhl Taghi. The locations of synoptic stations (dark blue triangle), tide gauges (red circle), wave buoys (blue rectangle) and weather radar (blue cylinder) close to the study area are shown in the map. The bathymetric data were derived from the General Bathymetric Chart of the Ocean (GEBCO) data combined with local hydrographic data available off the cities of Dayyer and Asaluyeh. Nakhl Taghi and Asaluyeh are in close proximity to each other and are located approximately 80 km from Dayyer

the so-called winter Shamal winds driving negative surges of approximately 0.25–0.4 m in the northernmost coastal regions (Thoppil and Hogan 2010) and (3) very rare or, more appropriately, tsunami occurrences from either local origin or propagating from the Indian Ocean are non-existent (Jordan 2008; Heidarzadeh et al. 2008). Consequently, waves of 2 to 3 metres hitting the south-eastern Bushehr (Fig. 1) Province shorelines located on the northern coast of the Persian Gulf in the morning hours of 19 March 2017 were an unprecedented and unexpected event. These waves resulted in substantial coastal inundation along the northern coasts of the Persian Gulf, including the cities of Dayyer, Nakhl Taghi and Asaluyeh (Fig. 1), causing death or injury to more than 20 people, severe damage to vessels and destruction of residential areas as well as coastal facilities. Given the extreme nature of the event, researchers such as Salaree et al. (2018) carried out several numerical simulations and extensive field surveys with the aim of better understanding the origin of these waves. Approximately 50 km of the Dayyer area coastline was thus surveyed two months after the event, and through eyewitness interviews and measurements of the eroded structures, the largest wave impacts and the inundations around the city of Dayyer were quantified. In addition, a multi-model approach was also performed to test the different possible sources of the observed waves (Okal et al. 2014), and Salaree et al. (2018) concluded that the seismic and landslide origin of the events had no capacity to generate

the observed intensity and distribution of the waves. As a geological origin of the event was discarded, a meteorological origin was also investigated by the authors with realistic numerical ocean simulations; however, due to unsatisfactory bathymetric data and meteorological forcing, the simulated extreme sea levels, even though qualitatively comparable to the observations, greatly underestimated the real impact of the waves. Further support for the meteorological origin of the event was provided by Heidarzadeh et al. (2020). Based on satellite imagery, atmospheric reanalysis products and in situ measurements, including sea level and high-resolution air pressure data recorded along the south of the Persian Gulf, resemblance between the observed high-frequency air pressure and sea level oscillations as well as synoptic patterns similar to those associated with the Mediterranean meteotsunamis (Šepić et al. 2015a) were found. Nevertheless, due to the lack of observations in the most affected areas and from the open sea during the event, the atmospheric disturbance that caused such strong waves was not properly quantified.

In the Persian Gulf, weather radar observations were not previously documented by Salaree et al. (2018) and Heidarzadeh et al. (2020) during the 2017 Dayyer event, and the mesoscale properties of the atmospheric disturbances that caused the destructive waves were not investigated. In this study, the meteotsunamigenic origin of the waves observed along the Dayyer coastline is studied in detail with 15-min time slices of weather radar observations from Bushehr; these observations are precise enough to document the propagation of the squall line and the associated convective cell and are combined with previously unpublished ground data and observations. Section 2 describes the event, while the atmospheric data used for the study are presented in Sect. 3. Section 4 overviews the observations at meteorological and sea level stations and presents an analysis of the synoptic patterns during the event. Section 5 provides weather radar observations, with a focus on the squall line responsible for the meteotsunami waves and their propagation over the open sea. Section 6 discusses the presented results, while concluding remarks are provided in Sect. 7.

## 2 Description of the studied area and 19 March 2017 event

A day before the Persian New Year, on 19 March 2017, approximately 100 km of the Persian Gulf's northern coast between the cities of Dayyer and Asaluyeh was affected by a sudden increase in sea levels, which led to inundations of coastal and urban areas. According to local observations, several long waves with regular crests approached the coast and first reached the beaches in Dayyer at approximately 8:00 local time (4:30 UTC). Photographs taken by eyewitnesses a few moments before the waves hit the coastline (Fig. 2) show these approaching waves at different locations. In addition to the Dayyer area, sudden sea level rises and significant coastal inundations were also recorded in the cities of Nakhil Taghi and Asaluyeh, which are located approximately 80 km east of Dayyer (Fig. 1). The waves reached Nakhil Taghi and Asaluyeh at 4:47 UTC, approximately twenty minutes after hitting the Dayyer area. Interestingly, videos recorded by eyewitnesses (<https://www.youtube.com/watch?v=1z0Zdl1mods>) indicate that several waves hit the coastline, with a 40–50-s period between their occurrences. These waves were presumably generated by the breaking off of the shoreline, where the bathymetry changes most rapidly. Precisely, the shelf is widest west of Dayyer, with depths up to 15 m stretching approximately 20 km from the coastline, while a depth of 15 m is reached in less than one kilometre off Nakhil Taghi and Asaluyeh. Furthermore, from the available photographs and videos, it can be deduced that the breaking occurred at a great distance from the coastline (from



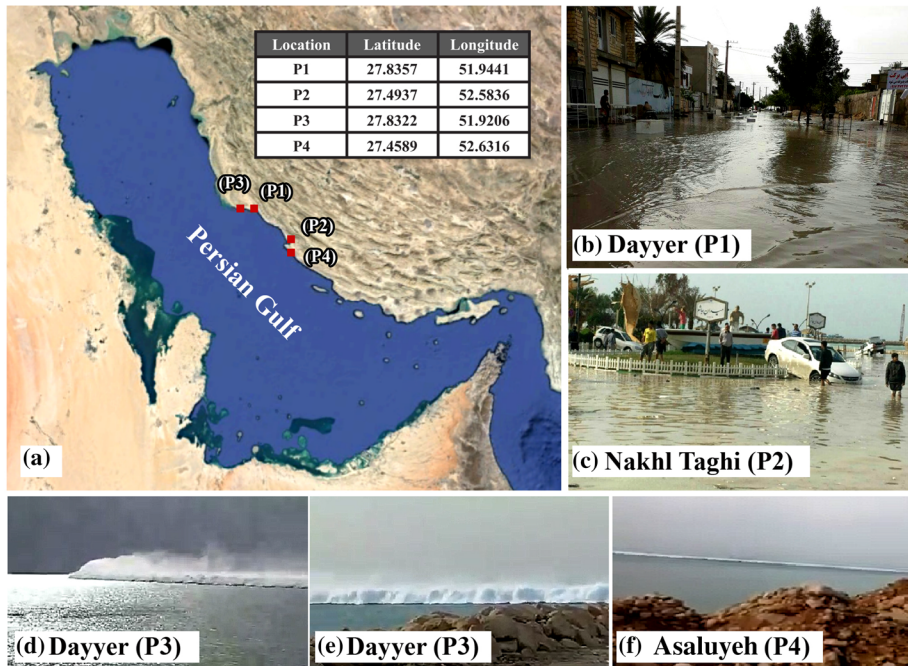


**Fig. 2** a Location of photographs taken by eyewitnesses and images of inundation of urban areas in b Dayyer (P1) (<https://www.yjc.ir/fa/news/6022024>) and c Nakhlaghi (P2) (<https://www.dana.ir/news/1067569.html>) and photographs of approaching waves along the d, e Dayyer (P3) (<https://www.namasha.com/v/QKJhgdg9>) and f Asaluyeh (P4) coastline on 19 March 2017

one-hundred metres to one kilometre) and generated tsunami bores approaching the shore in several places.

The eyewitness reports collected in this study document extreme waves over a greater area than that surveyed by Salaree et al. (2018), which was restricted to different parts of Dayyer, where a maximum run-up of 3 m and inundation of 600 m in the north-western part of the Dayyer suburbs were reported; these waves rapidly decreased in intensity in the eastern and western areas of the city. However, following recorded images (Fig. 3) and

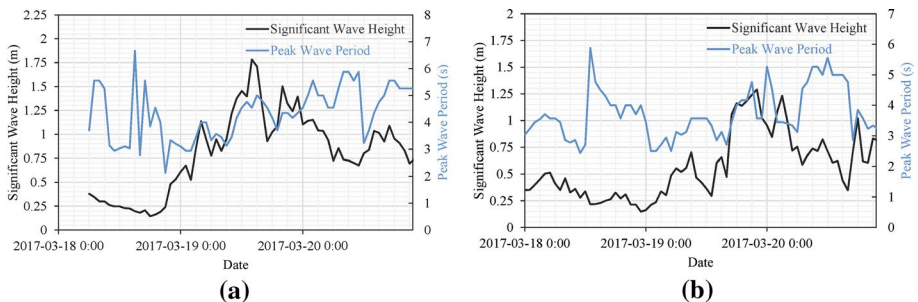


**Fig. 3** Measured significant wave heights and peak wave periods close to a Bushehr and b Kish Island by the Port and Maritime Organization (PMO) of Iran buoy network

data from tide gauges, the sudden sea level rises and subsequent coastal inundations also occurred in Asaluyeh and Nakhl Taghi, with characteristics (several consequent waves, propagating tsunami bore) identical to those observed in Dayyer. As a result of these sudden inundations, a number of local inhabitants and travellers along the coastal roads were seriously injured: a total of 22 injured and 5 missing persons were reported on 30 March in the morning, while two missing people were later found dead.

### 3 Data

The following in situ atmospheric and oceanic observations are used in this study:

1. Sea level observations were measured with a temporal resolution of 5 min during the period of the event at three tide gauges located at Asaluyeh, Bushehr (both operated by the Iranian Port and Maritime Organization) and Dayyer (operated by the Iranian National Cartographic Centre) (Fig. 1).
2. Wind-generated wave parameters were measured with a temporal resolution of 1 h at the Kish and Bushehr deep water wave buoys where the water depth is approximately 35 m (Fig. 1, operated by the Iranian Port and Maritime Organization).
3. Ground atmospheric station data were collected at the Bushehr, Dayyer and Asaluyeh stations (Fig. 1). The stations were not equipped with automatic devices at the time of the meteotsunami event, and weather data were thus recorded by an observer every hour at Asaluyeh and Bushehr and every three hours at Dayyer. At all stations, precipitation data were taken at synoptic terms (00, 03, ..., 21 UTC) and represent the cumulative value in the preceding 3 h.

In addition to these ground meteorological data, hourly ERA5 reanalysis results (<https://www.ecmwf.int/en/forecasts/datasets/reanalysis-datasets/era5>), which were produced by the European Centre for Middle-range Weather Forecast (ECMWF) with a 31-km resolution over the Persian Gulf, were used to analyse the general synoptic situation over the wide area of the northern Persian Gulf region.

Finally, the weather radar at Bushehr, which is operated by the Iranian Meteorological Organization and produces data every 15 min for an operational radius of 250 km covering most of the western and central parts of the Persian Gulf (Fig. 1), was used to quantify the meteotsunamigenic disturbance during the event. Hereafter, the following weather radar parameters are analysed: precipitation intensity (SRI), maximum reflectivity (MAX) and echo top height (ETH).

## 4 Oceanic and atmospheric observations

### 4.1 Sea level and wind wave analyses

As a detailed sea level analysis was performed by Heidarzadeh et al. (2020) during the meteotsunami event, only a succinct description is presented in this study. During 19 March 2017, several sharp oscillations, which were 1–2 m higher than the daily tidal levels and coinciding with reports of severe coastal flooding (Salaree et al. 2018), were observed at the Dayyer and Asaluyeh stations, while sharp oscillations were not captured

at the Bushehr sea water level station. The strength of the recorded oscillations is analysed with the de-tided (using T-TIDE software; Pawlowicz et al. 2002) and filtered (band-pass filter with a 2 h cut off period; Bendat and Piersol 1986) signals (not presented here). The maximum wave heights (crest-to-trough) of 2.03 m at Dayyer and 2.45 m at Asaluyeh were recorded at 4:30 UTC and 4:47 UTC and associated with periods of 15.5–18 min and 13.5–15.5 min, respectively. The calculated maximum wave heights are slightly higher than those presented by Heidarzadeh et al. (2020), which may be attributed to the application of different filter characteristics. Further analysis of sea level records performed by Heidarzadeh et al. (2020) shows that (1) the event was local, as tide gauges in Qatar, which are the only available data on the opposite coastline of the Persian Gulf, recorded oscillations with a maximum height of only 0.3 m and (2) both open ocean (at Dayyer) and harbour oscillations (at Asaluyeh) were recorded and presented similar distributions of energy, indicating the coherence between the observed sea level oscillations.

As documented previously (Heidarzadeh et al. 2020), in addition to the sharp sea level oscillations with dominant periods between 13.5 and 18 min, video recordings show several incoming waves or tsunami bores (i.e. hydraulic jump) developing a few hundred metres off the coast at specific locations and reaching the shore every 40–50 s. Due to the relatively low temporal resolution of the station measurements, these tsunami bores could not be recorded, and thus, real meteotsunami waves could be up to one metre higher than the recorded heights at the Dayyer and Asaluyeh stations. In addition, as the water is shallow close to the coastline and deepens further offshore, the observed generation of bores was presumably related to changes in water depth, as documented for the meteotsunami bore observed in south-western Sicily during the meteotsunami event on 25 June 2014 (Šepić et al. 2018a).

To support the hypothesis that observed bores were not generated by local winds, wind-induced wave records at two wave buoy stations, off Bushehr and at Kish (Fig. 1), were also analysed. As shown in Fig. 3, the significant wave heights (SWHs) varied between 0.5 and 1.0 m in height in the morning hours of 19 March 2017, indicating a sea state of 2 (SWH of 0.1–0.5 m) to 3 (SWH of 0.5–1.25 m) and moderate winds in the region. The observed SWH values were several times smaller than those documented for extreme events, in which the SWH may reach 4 m in March in the area of Asaluyeh (Kamranzad 2018). Relatively calm sea conditions with weak to moderate winds may also be seen in video recordings (<https://www.youtube.com/watch?v=1z0Zdl1mods>) during the approach of the meteotsunami bores.

## 4.2 Synoptic pattern and in situ meteorological observations

### 4.2.1 ERA5 reanalysis fields

The synoptic situation over the Persian Gulf and surrounding areas during the meteotsunami on 19 March 2017 is presented in Fig. 4 with mean sea level pressure, K-index instability parameter as well as geopotential height and relative vorticity at 500 hPa extracted from the ECMWF ERA5 reanalysis dataset at 00:00 and 04:00 UTC. Geopotential height and vorticity at 500 hPa were chosen to indicate the direction and intensity of the flow and convergence or divergence of air masses in the mid-troposphere, respectively. The K-index, which was introduced by George (1960), is related to the probability of occurrence of a potential thunderstorm and is defined as  $4 \times (K - 15)$ ; this index is based on the vertical temperature lapse rate and the amount and vertical extent of the low-level moisture in the

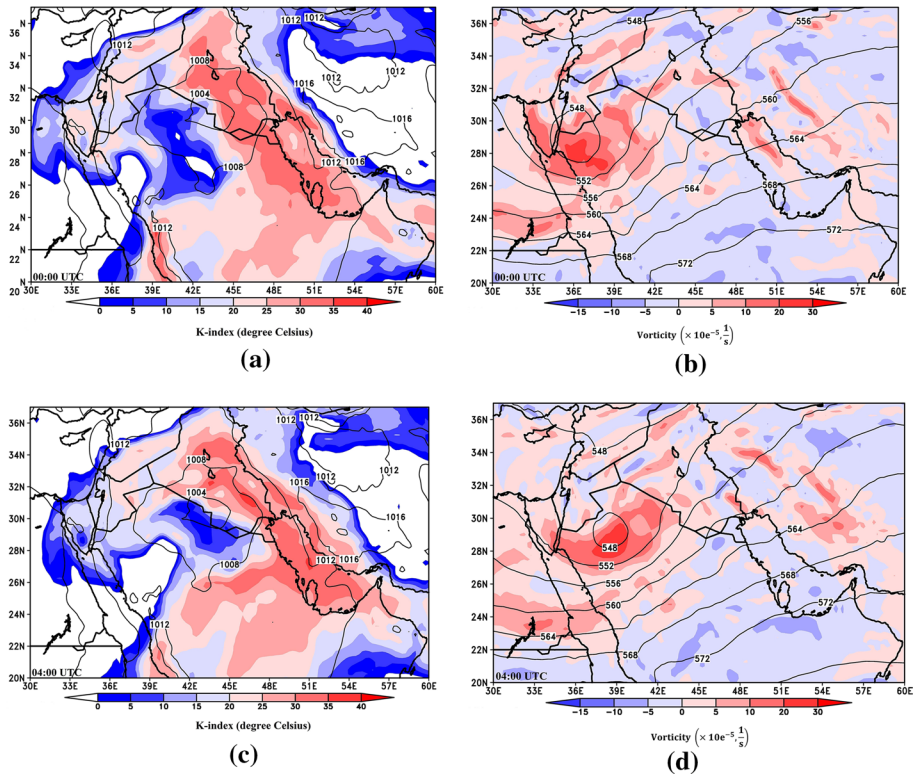


**Fig. 4** Mean sea level pressure and K-index at **a** 00:00 UTC and **b** 04:00 UTC (left column), geopotential height at 500 hPa (m) and vorticity ( $\times 10^{-5} \text{ s}^{-1}$ ) at **c** 00:00 UTC and **d** 04:00 UTC on 19 March 2017 (right column)

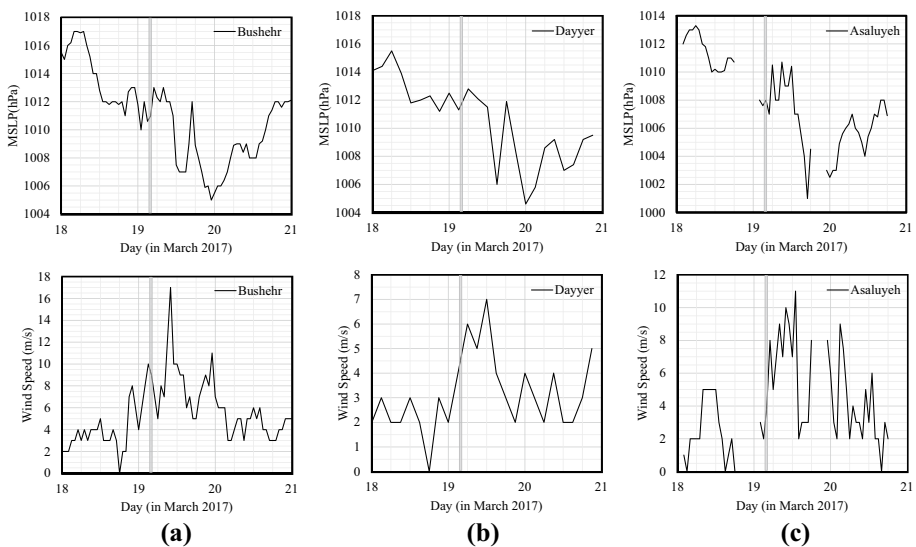
atmosphere. This analysis follows the findings by Heidarzadeh et al. (2020), who described a weak cyclone west that propagated eastward from the Persian Gulf during the 19 March 2017 event and was associated with (1) low-level inflow of warm and dry air on its frontal side and cold and humid air on the rear side, resulting in strong temperature and humidity gradients across the area, (2) a strong mid-tropospheric jet visible at 500 hPa, with wind speeds of up to 40 m/s over the Persian Gulf, and (3) a sand storm propagating over North Africa. Based on more recent reanalysis products (with high temporal and spatial resolutions) used in this study, the synoptic set-up can be described in more detail as follows: (1) at 00:00 UTC, a low-pressure system with a central pressure of 1004 hPa was present over the Persian Gulf region, while a 1016 hPa high-pressure system was located west of the Persian Gulf and north of the Strait of Hormuz, and a 60–80% probability of thunderstorm and strong convective cell occurrence were expected in the southern part of the Persian Gulf, where the K-index reached approximately 30–35 °C and (2) at 04:00 UTC, the whole system moved eastwards with K-index values above 35 °C, increasing the probability of thunderstorm occurrence to more than 80% over the limited area close to Dayyer and simultaneously, a deep trough extended to the south-east of the Mediterranean Sea and north-west of the Red Sea in the mid-troposphere at 500 hPa with positive relative vorticity, indicating persistent instabilities of the geopotential isolines west from the Persian

Gulf. Altogether, these synoptic conditions resemble synoptic conditions found during typical meteotsunami and high-frequency sea level oscillation events in the Mediterranean region (Šepić et al. 2015a, c).

#### 4.2.2 Synoptic station data

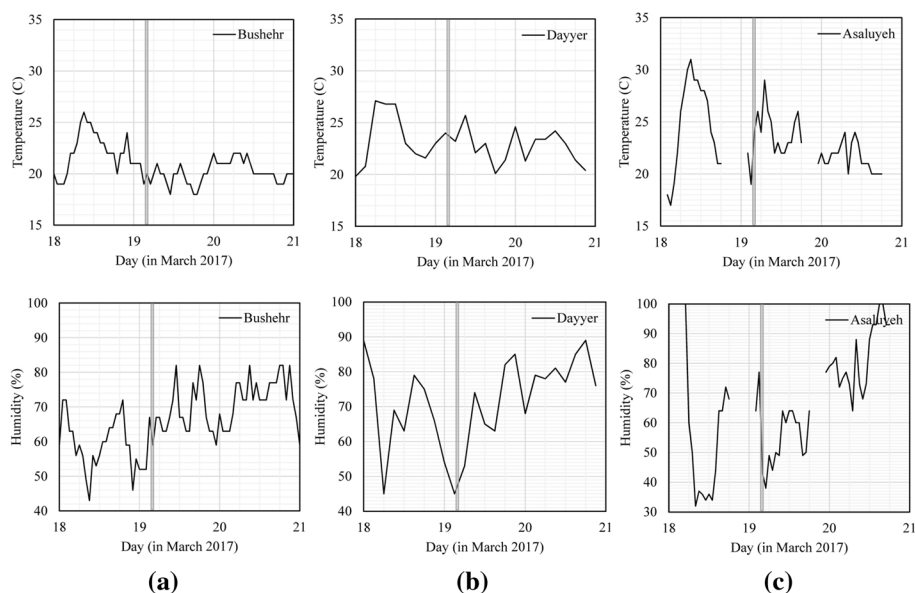
In situ observations of meteorological variables at the Bushehr, Dayyer and Asaluyeh synoptic stations (Figs. 5 and 6) reveal that the mean air pressure generally decreased between 18 and 19 March 2017, reaching its minimum value in the late hours of 19 March. Nevertheless, no pressure decrease was observed during the meteotsunami event itself, but rather significant hour-to-hour oscillations occurred with amplitudes of approximately 2 hPa at the Bushehr and Asaluyeh stations (oscillations can be seen even in Dayyer, where observations were carried out every three hours). During the morning hours of 19 March, the wind speed increased and reached values of 6–10 m/s at Bushehr and 4–8 m/s at Dayyer and Asaluyeh. The wind was even stronger, up to 16 m/s, after the event, when the cyclone and frontal zone approached the Persian Gulf. Air temperature data (Fig. 6) show no substantial changes during the meteotsunami event, except at Asaluyeh, where a sharp increase in temperature (of approximately 6 °C) associated with a sharp decrease in relative humidity from 75 to 40% can be seen. A drop in relative humidity during the event can also be seen at Dayyer but is not associated with air temperature changes, while a low relative humidity occurred at Bushehr a few hours before the meteotsunami event.

Figure 7 shows the reported weather conditions, including 3-h precipitation rates at 00:00, 06:00, 09:00, 12:00 and 18:00 UTC, at the studied synoptic stations between 18 and 19 March. While no significant precipitation was recorded on 18 March, dust carried by wind was reported at the Bushehr and Dayyer stations, and haze conditions were observed at the Asaluyeh station. On 19 March, precipitation (rain) of 1 mm at 00:00 UTC, 3 mm at



**Fig. 5** Wind speed at 10 m (m/s, bottom plots) and mean sea level pressure (hPa, upper plots) at the **a** Bushehr, **b** Dayyer and **c** Asaluyeh synoptic stations. The vertical grey line shows the time of the Dayyer meteotsunami





**Fig. 6** Temperature at 2 m (°C, upper plots) and relative humidity at 2 m (% , lower plots) at the **a** Bushehr, **b** Dayyer and **c** Asaluyeh synoptic stations. The vertical grey line shows the time of the Dayyer meteotsunami

06:00 UTC, 5 mm at 12:00 UTC and 5 mm at 18:00 UTC associated with thunderstorms after 15:00 UTC was recorded at the Bushehr station (Fig. 10a). At the Dayyer station, precipitation rates of 3 mm at 06:00 UTC, 10 mm at 12:00 UTC and 7 mm at 18:00 UTC with thunderstorm conditions were also recorded. Finally, precipitation observations at the Asaluyeh station were 0.6 mm at 00:00 UTC, 4 mm at 06:00 UTC, 0.4 mm at 12:00 UTC and 0.2 mm at 18:00 UTC, of which the observation at 06:00 UTC accounts for precipitation by the meteotsunamigenic squall line that passed over that region an hour before.

## 5 Weather radar imagery of meteotsunamigenic disturbances

The weak to moderate high-frequency sea level oscillations observed at the Dayyer and Asaluyeh tide gauges in the late evening hours of 18 March 2017 were linked by Heidarzadeh et al. (2020) to strong atmospheric convective activity over the Persian Gulf, which is visible on satellite images and confirmed by the weather conditions at synoptic stations (Fig. 7). To quantify this convective activity, surface rainfall intensity (SRI) radar images from Bushehr weather radar were analysed (Fig. 8). These images indicate that on 18 March the sky was clear until 15:00 UTC and no strong convective activity with precipitation took place during the late afternoon (not presented here). However, an intense convective system appeared in the evening when several storms were captured by weather radar images (Fig. 8). At 19:45 UTC, precipitation with a maximum intensity of approximately 15 mm/h occurred in the Persian Gulf, west of the Dayyer area. At 20:45 UTC, the maximum precipitation intensity increased to more than 30 mm/h before rapidly decreasing. At 22:00 UTC, the convective clouds reached waters off the



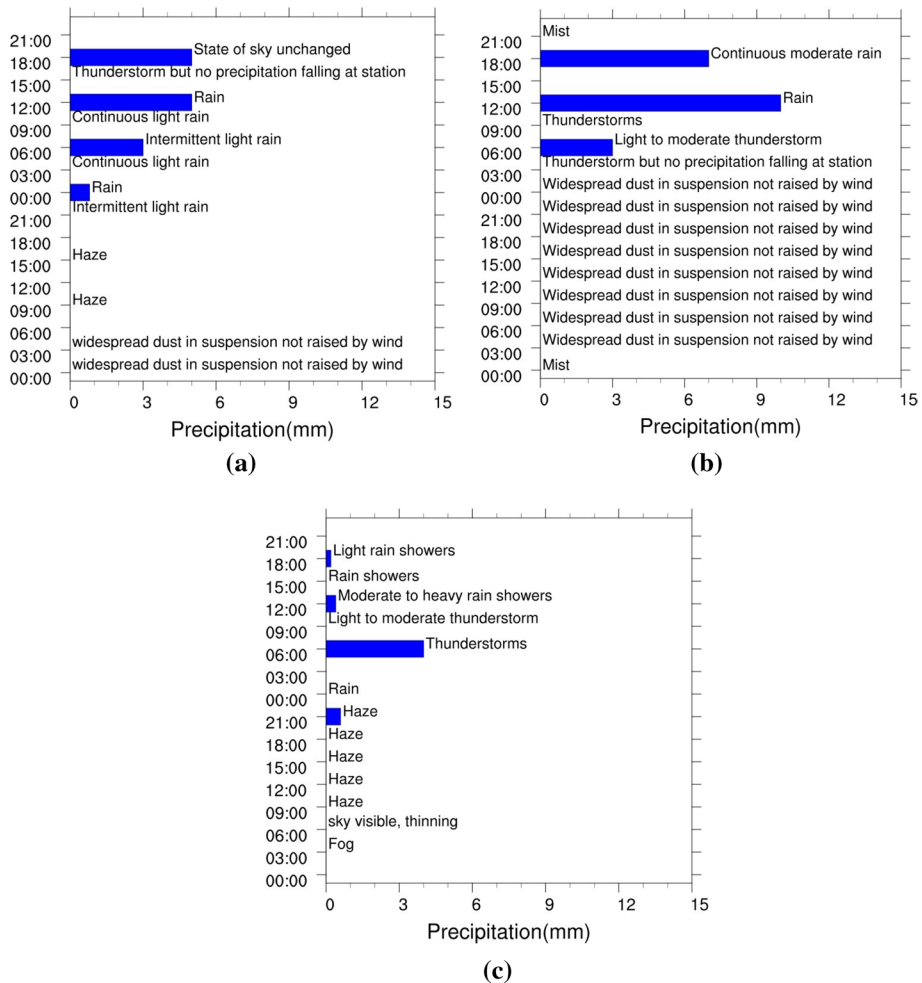


**Fig. 7** Precipitation (mm) and reported weather conditions at the **a** Bushehr, **b** Dayyer and **c** Asaluyeh stations between 18 and 19 March 2017

Dayyer area. Interestingly, moderate high-frequency sea level oscillations at Dayyer and Asaluyeh with 0.8–1.0 m wave heights were also measured between 22:30 and 23:00 UTC. The intense atmospheric convective activity continued through the night until the first hours on 19 March, when a new storm that was associated with precipitation of approximately 30 mm/h as detected by the SRI image at 0:15 UTC (Fig. 9) entered the Persian Gulf west from the Dayyer area. The convective system maintained its precipitation intensity on its way eastward until 1:45 UTC when it tilted in the NNW–SSE direction and formed an elongated and narrow system, indicating its transformation into an intense squall line. The size of the squall line as seen on the SRI precipitation images at 2:30 UTC (Fig. 9k, marked by black arrow) was ca. 70 km in length vs. 10 km in width, with a maximum precipitation intensity of more than 30 mm/h. The squall line further elongated to more than 130 km in length and narrowed to less than 10 km in width in the following two hours and hit Dayyer at 4:00 UTC (Fig. 9q) while still maintaining a

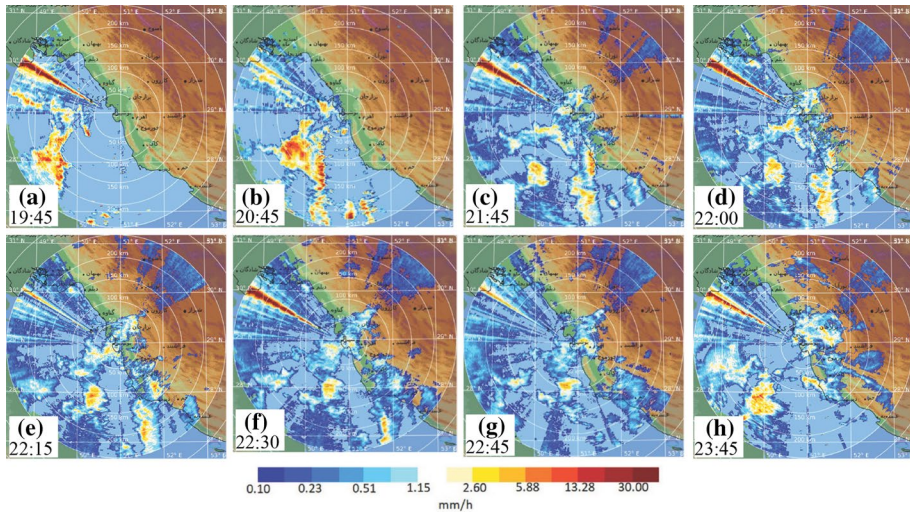


**Fig. 8** Precipitation intensity, SRI (in mm/h), from Bushehr radar images on 18 March 2017 (time is in UTC). The brown line in the north-western corner of all radar images is related to the radar noise

precipitation intensity greater than 30 mm/h. The squall line passed Asaluyeh 30 min later, at the exact time when the peak water level was observed at the tide gauge. Finally, the squall line lost its precipitation intensity when leaving the sea and crossing over land after 4:45 UTC (not shown).

In this study, the maximum reflectivity (MAX) weather radar images are also examined to further assess the intensity and structure of the convective clouds (Fig. 10) by studying the vertical and horizontal extents as well as the structure of the maximum reflectivity. A maximum reflectivity greater than 60 dBZ is usually a sign of intense convective clouds (Šepić and Rabinovich 2014). At 00:30 UTC (Fig. 10c), MAX images show that a convective cell associated with maximum reflectivity values of 60–64 dBZ was present in the south-western part of the domain, approximately 200 km west of Dayyer. High MAX values were restricted to the middle and upper troposphere, while no strong reflectivity values were found at heights below approximately 6 km. Through eastward movement of the convective system between 00:30 and 02:00 UTC, MAX values slightly decreased, while the vertical extent of the system was reduced and the lower base of the system dropped. At 02:30 UTC, the MAX values decreased to 48–52 dBZ, and the lower base of the convective system dropped below the detection limit (2 km) while extending vertically to approximately 5–6 km, indicating the transformation of the system to the squall line (Fig. 10k). The peak MAX values increased again to 52–56 dBZ at 03:30 UTC and up to 56–60 dBZ at 04:00 UTC, while the vertical extent of the system increased again to a height of approximately 9–12 km, indicating the development of a strong convective cell before hitting Dayyer. The lower base of high the MAX values again increased to approximately 3–5 km in height at 04:00 UTC. Indicatively, Wertman et al. (2015) showed the correlation between radar reflectivity and atmospheric pressure anomalies so that the largest positive pressure anomalies occur where reflectivity is greater than 40 dBZ. Since the reflectivity values in the observed squall line and convective cell are greater than 40 dBZ over the whole trajectory of the system, an intense air pressure disturbance was presumably present and attached to the system on its path over the sea during 19 March 2017.

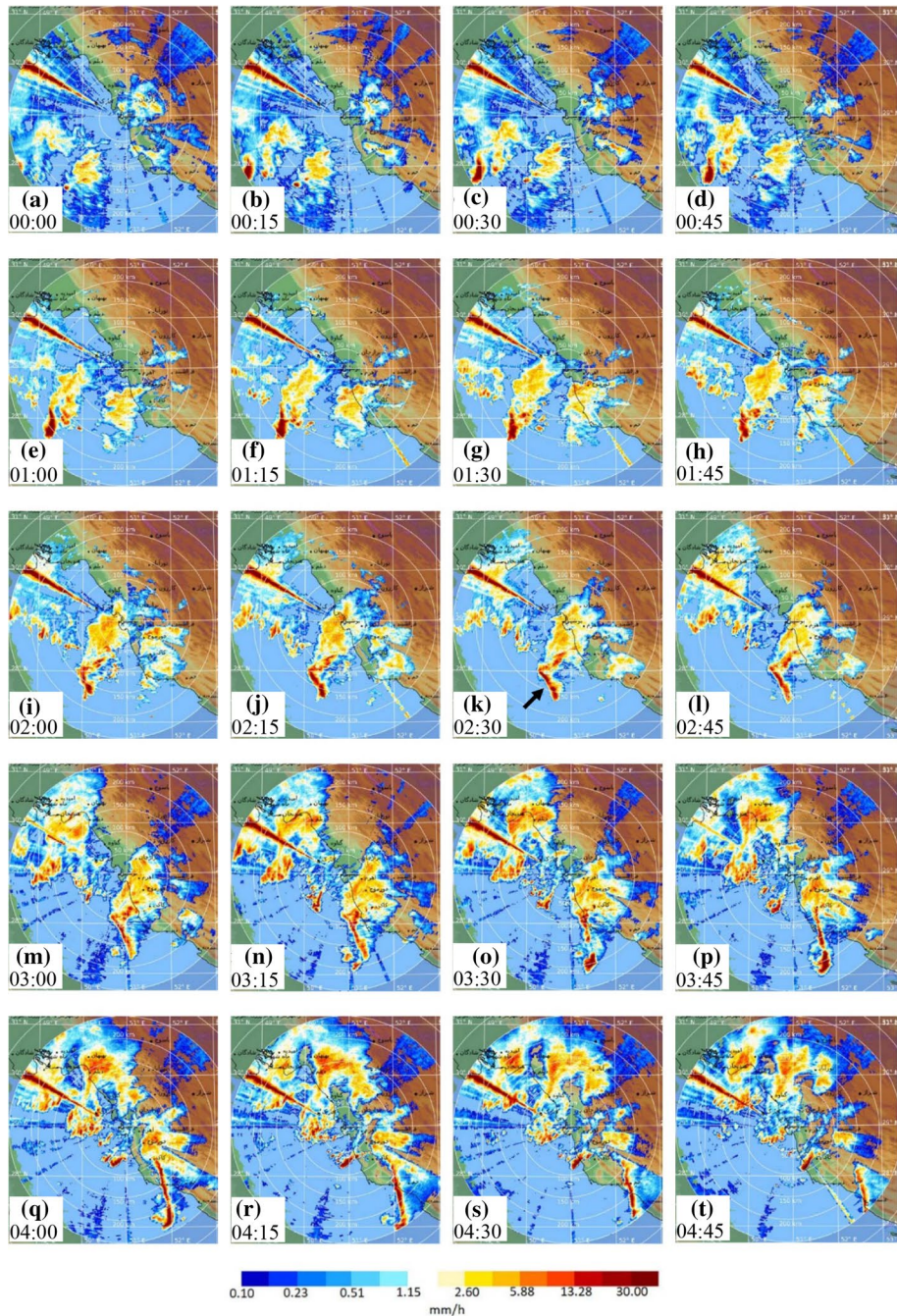


**Fig. 9** Precipitation intensity, SRI (mm/h), from the Bushehr weather radar on 19 March 2017 mapped every 15 min from 0:00 UTC (a) to 4:45 UTC (t). The brown line in the north-west of all radar images is related to the radar noise



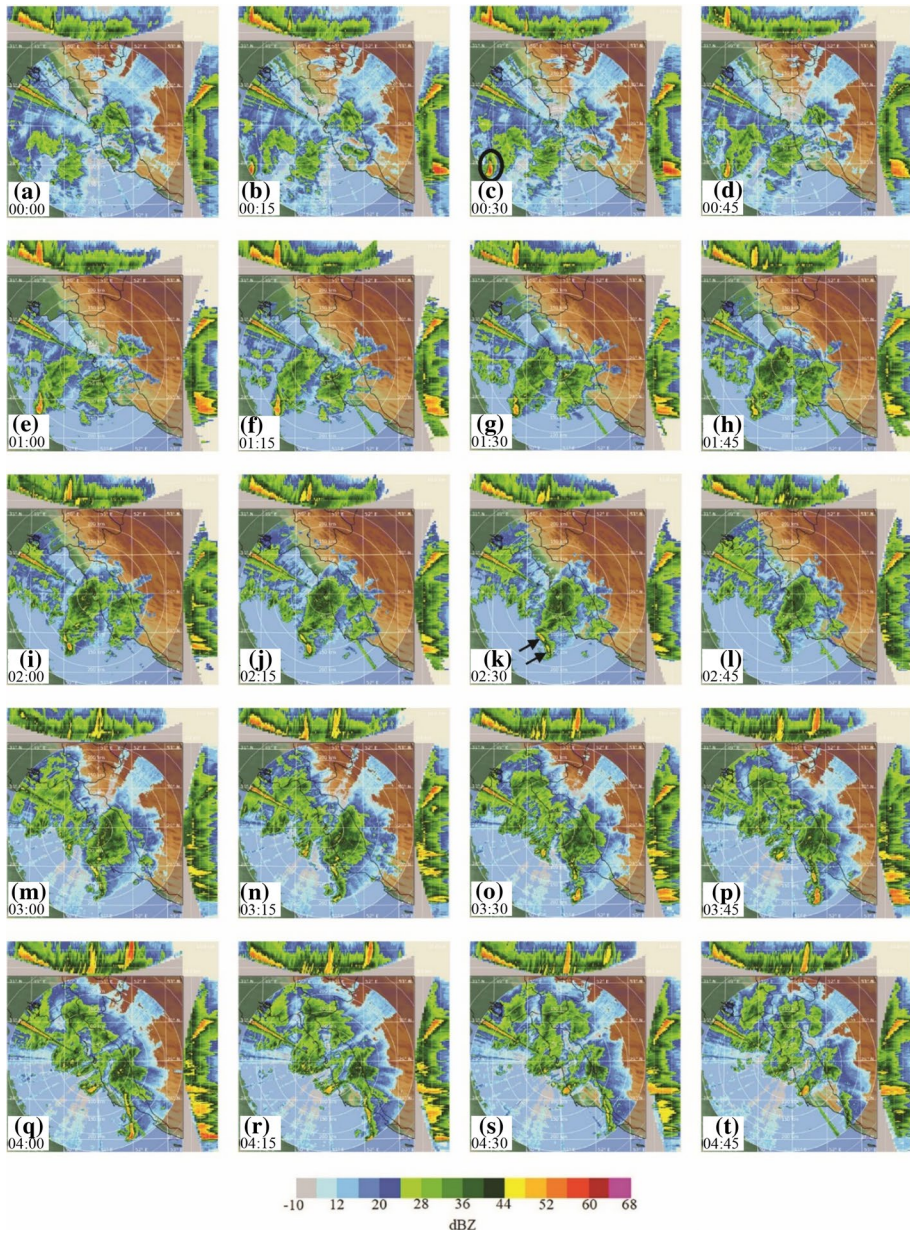


**Fig. 10** Maximum reflectivity, MAX (dBZ), from the Bushehr weather radar on 19 March 2021 mapped every 15 min from 0:00 UTC (a) to 4:45 UTC (t). The central image represents the maximum vertical reflectivity values, while side plots display the maximum latitudinal and longitudinal reflectivity values. The upper height of the side plots is at 12 km. The entrance of the convective system to the Persian Gulf is indicated by an ellipse at 00:30 UTC, while it transforms to a squall line at 02:30 UTC. The brown line in the north-west of all radar images is related to the radar noise

The final weather radar product examined during the meteotsunami event was the echo top height (ETH) values, which indicate the maximum vertical height of convective systems in an area (Fig. 11). This parameter is widely used to quantify the severity of

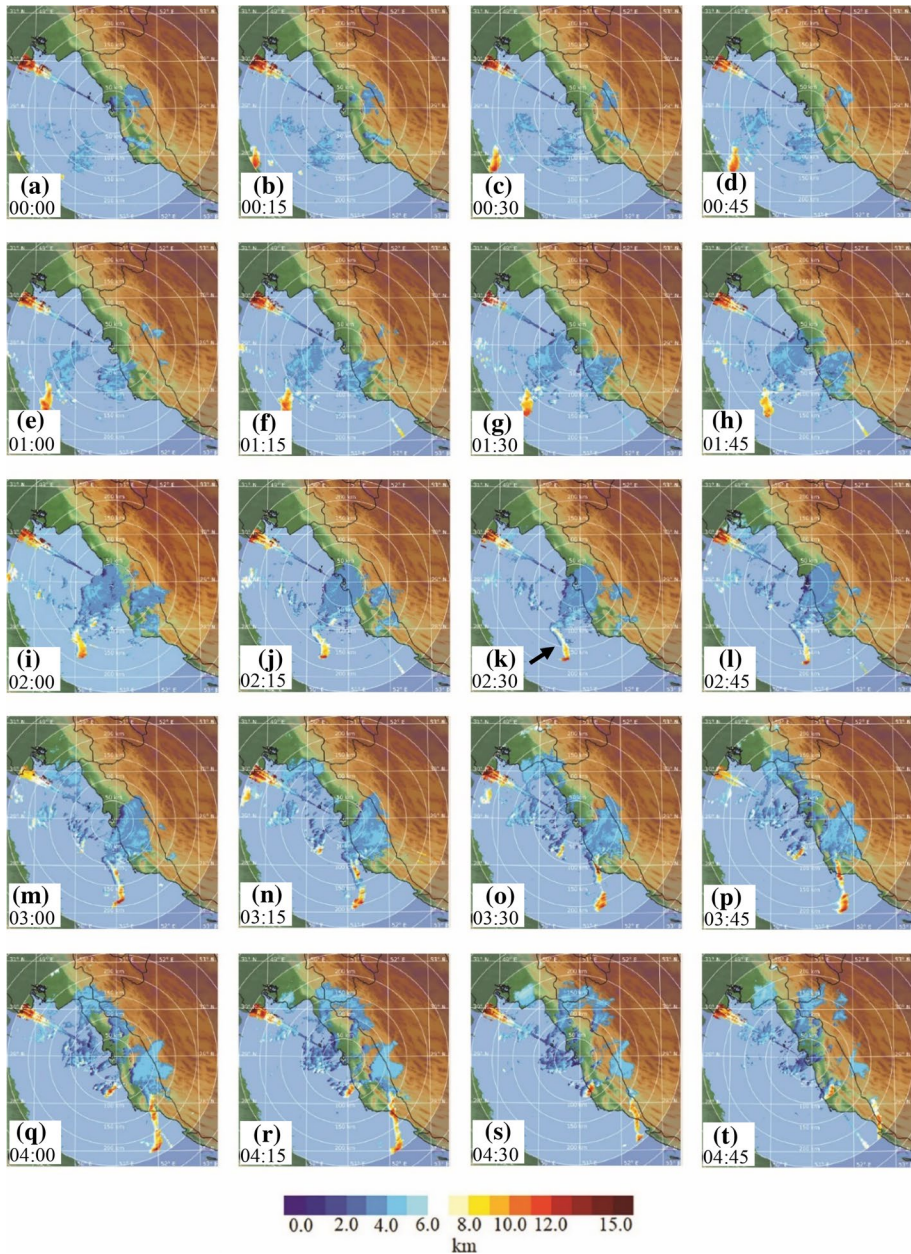


**Fig. 11** Echo top height, ETH (km), from the Bushehr weather radar on 19 March 2017 mapped every 15 min, from 0:00 UTC (a) to 4:45 UTC (t). The brown line in the north-west of all radar images is related to the radar noise



mesoscale weather systems for aviation applications (Delobbe and Holleman 2006; Lakshmanan et al. 2013). Upon entering the Persian Gulf, the maximum ETH values of the convective system were at approximately 12 km (at 00:30 UTC, Fig. 11c). The ETH values decreased upon the transition of the mesoscale system to the squall line, reaching values of approximately 7–9 km at 02:30 UTC (Fig. 11k) in the northern section of the line while peaking at values higher than 12 km in the narrow band at the southern edge of the system (marked by arrow in Fig. 11k). Except at the southernmost segment of the squall line, ETH values were low in the following 45 min, and they again started to rise to values higher than 10 km after 03:30 UTC. Such values remained until the squall line hit land. Interestingly, all other connective systems to the north of the meteotsunamigenic squall line were restricted mostly to the lower and mid-troposphere (ETH values up to 5 km, Fig. 11f–n).

## 6 Discussion

The analysis of Bushehr weather radar images revealed that the meteotsunami event on 19 March 2017 was generated by an atmospheric mesoscale convective system travelling eastward above the sea for approximately 4 h before hitting the Dayyer coastal region. The system transformed into an intense and narrow squall line in the middle of the sea, which was presumably associated with a sharp change in air pressure, as previously documented (Churchill et al. 1995; Paxton and Sobien 1998; Šepić and Rabinovich 2014). The squall line was conjoined with intense but short-lasting precipitation, thus being visible on images of precipitation intensity captured by the weather radar. The occurrence of precipitation during meteotsunamigenic disturbances is not necessarily the case during severe meteotsunamis, particularly those generated by wave-ducting mechanisms (Monserrat and Thorpe 1996). In addition, Wertman et al. (2015) found that a radar reflectivity of approximately 60 dBz is generally associated with air pressure increases higher than 3 hPa and up to 6 hPa. Aside from the intensity of the meteotsunamigenic disturbance, horizontal gradients (and the equivalent temporal rate of change) greatly impact meteotsunami waves: the higher the horizontal gradient and temporal rate of change are, the higher the meteotsunami wave growth (Vilibić 2008; Williams et al. 2020). For the 19 March 2017 meteotsunami event in Dayyer, the squall line was no wider than 10 km once it reached the middle of the Persian Gulf, which indicates that it was associated with extremely sharp pressure changes. Finally, the persistence of the convective system and the squall line was high, indicating low dissipation of energy and high self-maintenance of the system (Belušić et al. 2007).

Another important process for the generation of a destructive meteotsunami is the resonant transfer of energy from atmospheric disturbance to the sea, presumably occurring through the Proudman resonance (Proudman 1929) as the disturbance travelled over a flat region. The Proudman resonance occurs when the speed of the atmospheric disturbance ( $U$ ) becomes equal to the speed of the long ocean waves ( $c = \sqrt{gh}$ , where  $g$  is gravity and  $h$  is water depth). Figure 12 indicates the propagation speed (numbers) and extension (black line) of the squall line over time at 15-min intervals, which were estimated from weather radar observations (the propagation speed is the average for the whole squall line). The speed estimated from weather radar observations ranged from approximately 22 m/s when the convective system reached the central part of the Persian Gulf (approximately 02:30 UTC) to approximately 25 m/s when the system hit the cities of Dayyer and Asaluyeh (Fig. 12), occasionally reaching a value of 27.0 m/s. The squall line also tilted clockwise



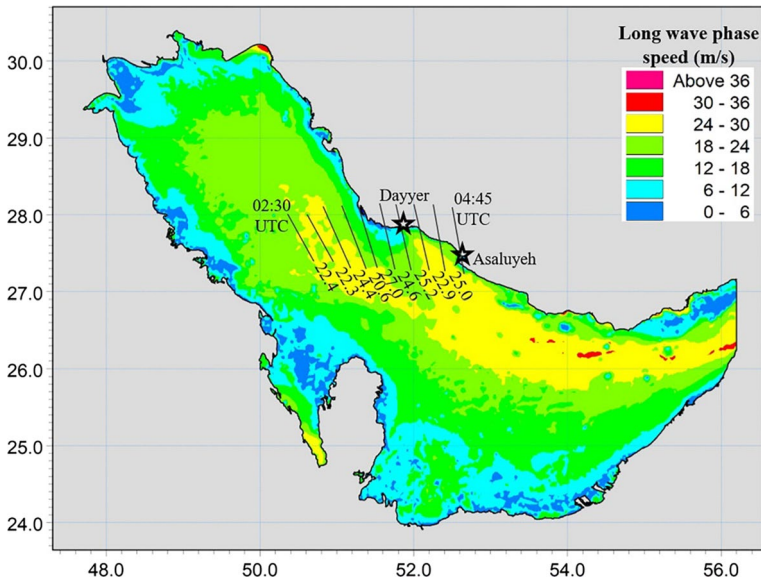


**Fig. 12** Average propagation speed (numbers) and extension of the squall line (lines) over the Persian Gulf on 19 March 2017 from 02:30 to 04:45 UTC estimated from weather radar observations. The colours on the map show the distribution of the longwave phase speed in the Persian Gulf

between 3:00 and 3:45 UTC, when the average squall line speed decreased to 20.6 m/s and was lowest at the southern perimeter of the line. The propagation speeds match the speeds of long ocean waves in a great part of the area over which the atmospheric disturbance travelled (Fig. 12). These long wave phase speeds were estimated using the General Bathymetric Chart of the Ocean (GEBCO) data combined with local hydrographic data available in the vicinity of the Dayyer and Asaluyeh areas.

If assuming full resonance conditions, meteotsunami waves may grow following a simple formula (Hibiya and Kajiura 1982; Monserrat et al. 2006):

$$\Delta\zeta = \frac{\Delta\bar{\zeta}}{L_1} \frac{x_f}{2}$$

where  $x_f = U \cdot t$  is the distance travelled by the pressure jump during time  $t$ ,  $L_1$  is the width of the disturbance (from its edge to the centre, or the area of maximum air pressure change), and  $\Delta\bar{\zeta}$  is the inverse barometric ocean response, which is equal to 1 cm for an air pressure jump of 1 hPa. Assuming that resonant conditions were persistent over  $x_f = 100$  km, with  $L_1$  equals 5 km (half-width of the squall line) and  $\Delta\bar{\zeta} = 6$  cm, the total amplification of the meteotsunami waves through the Proudman resonance would be approximately 60 cm. The  $\Delta\bar{\zeta}$  value was chosen arbitrarily following documented values for severe meteotsunamigenic disturbances (e.g. Vilibić et al. 2004) as no microbarograph measurements were available along the pathway of the squall line; however, this value is much lower than that used in numerical modelling by Salaree et al. (2018), who used a pressure jump of 15 hPa in their modelling exercises. The amplification through a Proudman resonance of 60 cm might be higher if the asymmetry of the squall line is considered (i.e. the pressure change may not be the highest at the centre of the line). However, this estimated value supports

the study by Heidarzadeh et al. (2020), which (1) assumed that amplification through Proudman resonance was ca. 80 cm without any detailed knowledge of the shape or size of the disturbance and (2) explained the final observed wave amplification to a height of 230 cm through bathymetry shallowing effects known to also occur during regular tsunamis; however, this study did not consider the observed wave breaking and the tsunami bore. These simplified estimates should be confirmed with ultra-high-resolution modelling efforts, including sub-kilometre grids in the atmosphere and ocean grid or mesh reaching 10 metres or lower in the Dayyer coastal region. For such modelling studies, setting up the proper atmospheric disturbance speed is crucial to quantify the Proudman resonance and reproduce the observed meteotsunami waves; a change in just 2 m/s may double or reduce to half the height of the meteotsunami wave (Šepić et al. 2015b).

The ratio of the atmospheric disturbance speed  $U$  and the speed of long ocean waves  $c$ , which is referred to as the Froude number  $Fr$ , is found to control the efficiency of the Proudman resonance (Šepić et al. 2015a; Williams et al. 2020). To quantify the sensitivity of the Proudman resonance to the atmospheric disturbance propagation speed, three different speeds of 20.6 m/s, 23.8 m/s and 27.0 m/s (minimum, average and maximum average propagation speed of squall line, respectively, presented in Fig. 12) were tested (Fig. 13). The results of the sensitivity study show that (1) most of the shallow area off the Dayyer coastal region (marked by ellipse) is not favourable for low- or high-speed scenarios, (2) Proudman resonance conditions ( $0.8 < Fr < 1.2$ ) that extend over lengths greater than 120 km are fulfilled for the 23.8 m/s

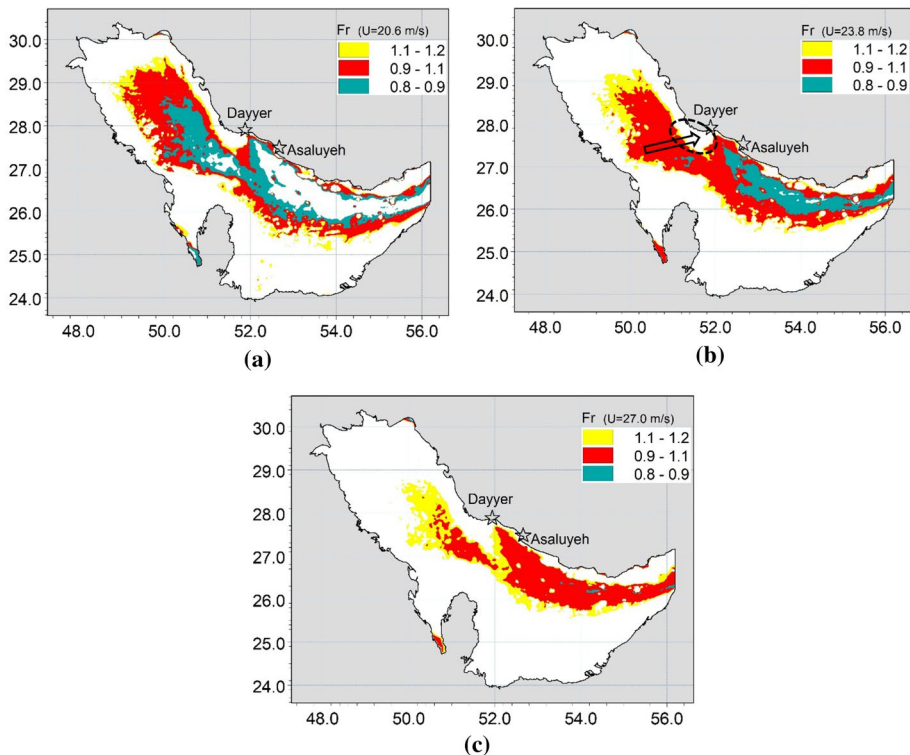


**Fig. 13** Meteotsunami-favourable areas in the Persian Gulf for which  $0.8 < Fr < 1.2$  for **a**  $U=20.6$  m/s, **b**  $U=23.8$  m/s and **c**  $U=27.0$  m/s

scenario similar to the observed squall line speed during the 19 March 2017 Dayyer meteotsunami, and (3) the conditions for efficient Proudman resonance off Asaluyeh (and along the coastline south-east of Asaluyeh) are acquired for increased speed, as observed during the 19 March 2017 event in which the speed of the squall line increased when approaching Asaluyeh. Our results are in agreement with the results by Heidarzadeh et al. (2020), who provided the respective sensitivity maps based on the proxy disturbance speed value coming from ERA-Interim reanalysis winds at 500 hPa, pointing to the appropriateness of using this proxy when estimating the ground propagation speed, as found during a large number of meteotsunami events (e.g. Monserrat and Thorpe 1996; Šepić et al. 2015a). On the other hand, idealized simulations by Salaree et al. (2018) provided the strongest resonance conditions for meteotsunamigenic disturbances coming from NNW with a speed of 10 m/s. Nevertheless, the domain of their simulation does not cover the central and western parts of the area over which the observed squall line travelled and over which the full resonant conditions were reached. Furthermore, it remains a question whether the speed and propagation direction of the squall line represent the worst-case scenario causing the maximum wave heights, as a range of propagation directions and speeds may result in a destructive meteotsunami (Orlić et al. 2010; Ličer et al. 2017).

In summary, this study quantifies the shape, size and intensity of atmospheric disturbances during the 19 March 2017 meteotsunami event with weather radar images, which proved to better capture mesoscale structures than classical in situ or satellite measurements and should be more widely used in meteotsunami research. The use of ground observations to better quantify weather radar parameters has been proven to be a necessity to properly characterize meteotsunamigenic disturbances and might be properly tested in regions with relatively dense networks of meteorological measurements at a fine resolution (Rabinovich et al. 2020). In this case, parameters of the meteotsunamigenic disturbances extracted from calibrated weather radar may be used in process-oriented modelling studies with the aim of better representing the generation and amplification of the meteotsunami waves as well as precisely assessing their associated hazards and risks.

Process-oriented studies may elucidate the magnitude of the air pressure jump, which is a crucial ingredient for any meteotsunami, as well as the rate of change or air pressure gradients that best fit the observed ocean response while being associated with the convective system. To quantify such forcing, a coupled atmosphere–ocean numerical model should be adopted with the aim of properly reproducing the meteotsunami dynamics. In practice, these processes are occurring in the atmosphere at less than a 5-km scale, which implies the need for an ultra-high-resolution atmospheric model at a resolution of approximately one kilometre. For oceans, the model resolution should be even higher, as it is shown for similar bathymetries that a horizontal resolution of several metres is a prerequisite to properly capture the coastal dynamics (Linares et al. 2019). In this sense, proper reproduction of meteotsunamigenic disturbances driving meteotsunami waves is at the forefront of the capacities of the available tools in atmospheric and ocean research, and the 19 March 2017 northern Persian Gulf event may be an excellent test case for developing new solutions applicable for processes at ultra-high resolution.

## 7 Conclusions

The destructive meteotsunami that occurred on 19 March 2017 along the northern coast of the Persian Gulf was investigated using observations, including the first use of weather radar imagery to elucidate the atmospheric origin of the event. Indeed, previous studies by Salaree et al. (2018) and Heidarzadeh et al. (2020) linked the phenomenon to intense fluctuations in air pressure but could not provide any details about the meteotsunamigenic disturbance as not using the appropriate observation tools. This study thus bridges this gap with 15-min weather radar observations covering the entire area affected by the travelling atmospheric disturbance and is used to characterize the evolution in the structure and intensity of the convective system. In addition, several new atmospheric and oceanic datasets, including data from synoptic stations, ECMWF ERA5, wave buoys and tide gauges, were used in addition to weather radar observations. The following conclusions were reached:

- Wind wave observations and available videos showed that a calm sea prevailed at the time of the meteotsunami event with measured wave heights of up to 2.5 m on which several incoming waves in the form of tsunami bores superimposed and reached the coastline every 40–50 s; thus, the bathymetry changes off Dayyer and Asaluyeh were responsible for the formation of the observed tsunami bores. Thus, the total height of the meteotsunami waves was up to one metre higher than that measured at the tide gauges.
- In the early hours of 19 March 2017, the instability parameter K-index extracted from ERA5 was extremely high, indicating a high probability of occurrence of thunderstorms and convective systems over the Persian Gulf, especially close to the Dayyer and Asaluyeh areas. Synoptic station data in these areas also indicated the occurrence of a thunderstorm at the time of the events.
- SRI radar images indicated that a moderate meteotsunami event observed at Dayyer with a crest-to-trough height of approximately 0.8–1.0 metres in the last hours of 18 March 2017 was also associated with the eastward travel of a convective mesoscale system over the Persian Gulf.
- SRI, MAX and ETH radar images clearly showed that the intense atmospheric mesoscale convective system is the main atmospheric origin of the northern Persian Gulf meteotsunami that occurred in the early hours of 19 March 2017. The system entered the Persian Gulf 4 h before the event, transforming from mid- and upper troposphere convective storms to an elongated and extremely narrow squall line and maintaining its high reflectivity throughout the sea trajectory.
- The average travel speed of the meteotsunamigenic disturbance estimated from weather radar images was approximately 24 m/s, which matched the speed of long ocean waves over 120 km in the central Persian Gulf and provided favourable conditions for resonant pumping of energy from the atmosphere to the sea through the Proudman resonance.

**Acknowledgements** The synoptic data and weather radar data were provided by I.R. of the Iran Meteorological Organization. The tide gauge data and wave buoy data were provided by the National Cartographic Centre (NCC) of Iran and the Port and Maritime Organization (PMO) of Iran, respectively. ERA5 reanalysis data produced by the European Centre for Medium-range Weather Forecast (ECMWF) were taken from <https://www.ecmwf.int/en/forecasts/datasets/reanalysis-datasets/era5>. The authors are very thankful to eyewitness photographers who provided the images presented in Fig. 2. The comments raised by two anonymous reviewers are strongly appreciated. The first author would like to thank the Iran National Science

Foundation (INSF) for funding this research under Project No. 96000740. Work by I.V. and C.D. has been supported by the Croatian Science Foundation (Project ADIOS, Grant No. IP-2016-06-1955).

## Compliance with ethical standards

**Conflict of interest** The authors declare that they have no conflict of interest.

## References

- Akbari P, Sadrinasab M, Chegini V, Siadatmousavi SM (2016) Tidal constituents in the Persian Gulf, Gulf of Oman and Arabian Sea: a numerical study. *Indian J Mar Sci* 45:1010–1016
- Bechle AJ, Wu CH, Kristovich DAR, Anderson EJ, Schwab DJ, Rabinovich AB (2016) Meteotsunamis in the Laurentian Great Lakes. *Sci Rep* 6:37832. <https://doi.org/10.1038/srep37832>
- Belušić D, Grisogono B, Klaić ZB (2007) Atmospheric origin of the devastating coupled air–sea event in the east Adriatic. *J Geophys Res* 112:D17111. <https://doi.org/10.1029/2006JD008204>
- Bendat JS, Piersol AG (1986) Random data: analysis and measurement procedures. Wiley, New York
- Churchill DD, Houston SH, Bond NA (1995) The Daytona Beach wave of 3–4 July 1992: a shallow water gravity wave forced by a propagating squall line. *Bull Am Meteorol Soc* 76:21–32. [https://doi.org/10.1175/1520-0477\(1995\)076%3c0021:TDBWOJ%3e2.0.CO;2](https://doi.org/10.1175/1520-0477(1995)076%3c0021:TDBWOJ%3e2.0.CO;2)
- Delobbe L, Holleman I (2006) Uncertainties in radar echo top heights used for hail detection. *Meteorol Appl* 13(4):361–374. <https://doi.org/10.1017/S1350482706002374>
- Dragani WC, D’Onofrio EE, Oreiro F, Alonso G, Fiore M, Grismeyer W (2014) Simultaneous meteorological tsunami and storm surges at Buenos Aires coast, southeastern South America. *Nat Hazards* 74:269–280. <https://doi.org/10.1007/s11069-013-0836-2>
- Ewing M, Press F, Donn WL (1954) An explanation of the Lake Michigan wave of 26 June 1954. *Science* 120:684–686. <https://doi.org/10.1126/science.120.3122.684>
- George JJ (1960) Weather forecasting for aeronautics. Academic Press, New York, p 673
- Greenspan HP (1956) The generation of edge waves by moving pressure distributions. *J Fluid Mech* 1:575–592. <https://doi.org/10.1017/S002211205600038X>
- Heidarzadeh M, Pirooz MD, Zaker NH, Yalciner AC, Mokhtari M, Esmaeili A (2008) Historical tsunami in the Makran Subduction Zone off the southern coasts of Iran and Pakistan and results of numerical modeling. *Ocean Eng* 35(8–9):774–786. <https://doi.org/10.1016/j.oceaneng.2008.01.017>
- Heidarzadeh M, Šepić J, Rabinovich A, Allahyar M, Soltanpour A, Tavakoli F (2020) Meteorological tsunami of 19 March 2017 in the Persian Gulf: observations and analyses. *Pure Appl Geophys* 177:1231–1259. <https://doi.org/10.1007/s00024-019-02263-8>
- Hibiya T, Kajiura K (1982) Origin of ‘Abiki’ phenomenon (a kind of seiche) in Nagasaki Bay. *J Oceanogr Soc Jpn* 38:172–182. <https://doi.org/10.1007/BF02110288>
- Jordan BR (2008) Tsunamis of the Arabian Peninsula: a guide of historic events. *Sci Tsunami Hazards* 27(1):31–46
- Kamranzad B (2018) Persian Gulf zone classification based on the wind and wave climate variability. *Ocean Eng* 169:604–635. <https://doi.org/10.1016/j.oceaneng.2018.09.020>
- Lakshmanan V, Hondl K, Potvin CK, Preignitz D (2013) An improved method for estimating radar echo-top height. *Weather Forecast* 28:481–488. <https://doi.org/10.1175/WAF-D-12-00084.1>
- Ličer M, Mourre B, Troupin C, Kriemeyer A, Jansá A, Tintoré J (2017) Numerical study of Balearic meteotsunami generation and propagation under synthetic gravity wave forcing. *Ocean Model* 111:38–45. <https://doi.org/10.1016/j.ocemod.2017.02.001>
- Linares Á, Wu CH, Bechle AJ, Anderson EJ, Kristovich DAR (2019) Unexpected rip currents induced by a meteotsunami. *Sci Rep* 9:2105. <https://doi.org/10.1038/s41598-019-38716-2>
- Lipa B, Parikh H, Barrick D, Roarty H, Glenn S (2014) High-frequency radar observations of the June 2013 US East Coast meteotsunami. *Nat Hazards* 74:109–122. <https://doi.org/10.1007/s11069-013-0992-4>
- Mafi-Gholami D, Zenner EK, Jaafari A, Riahi-Bakhtiari H, Bui DT (2019) Multi-hazards vulnerability assessment of southern coasts of Iran. *J Environ Manag.* <https://doi.org/10.1016/j.jenvman.2019.109628>
- Montserrat S, Thorpe AJ (1996) Use of ducting theory in an observed case of gravity waves. *J Atmos Sci* 53:1724–1736. [https://doi.org/10.1175/1520-0469\(1996\)053%3c1724:UODTIA%3e2.0.CO;2](https://doi.org/10.1175/1520-0469(1996)053%3c1724:UODTIA%3e2.0.CO;2)


- Monserat S, Vilibić I, Rabinovich AB (2006) Meteotsunamis: atmospherically induced destructive ocean waves in the tsunami frequency band. *Nat Hazards Earth Syst Sci* 6:1035–1051. <https://doi.org/10.5194/nhess-6-1035-2006>
- Okal EA, Visser JNJ, de Beer CH (2014) The Dwarskersbos, South Africa local tsunami of August 27, 1969: field survey and simulation as a meteorological event. *Nat Hazards* 74:251–268. <https://doi.org/10.1007/s11069-014-1205-5>
- Orlić M, Belušić D, Janeković I, Pasarić M (2010) Fresh evidence relating the great Adriatic surge of 21 June 1978 to mesoscale atmospheric forcing. *J Geophys Res* 115:C06011. <https://doi.org/10.1029/2009JC005777>
- Pattiaratchi CB, Wijeratne EMS (2015) Are meteotsunamis an underrated hazard? *Philos Trans R Soc A* 373:20140377. <https://doi.org/10.1098/rsta.2014.0377>
- Pawlowicz R, Beardsley B, Lentz S (2002) Classical tidal harmonic analysis including error estimates in MATLAB using T\_TIDE. *Comput Geosci* 28(8):929–937. [https://doi.org/10.1016/S0098-3004\(02\)00013-4](https://doi.org/10.1016/S0098-3004(02)00013-4)
- Paxton CH, Sobien DA (1998) Resonant interaction between an atmospheric gravity wave and shallow water wave along Florida's west coast. *Bull Am Meteorol Soc* 79:2727–2732. [https://doi.org/10.1175/1520-0477\(1998\)079%3c2727:RIBAAG%3e2.0.CO;2](https://doi.org/10.1175/1520-0477(1998)079%3c2727:RIBAAG%3e2.0.CO;2)
- Proudman J (1929) The effects on the sea of changes in atmospheric pressure. *Geophys Suppl Mon Not R Astron Soc* 2(4):197–209. <https://doi.org/10.1111/j.1365-246X.1929.tb05408.x>
- Rabinovich AB (2020) Twenty-seven years of progress in the science of meteorological tsunamis following the 1992 Daytona Beach event. *Pure Appl Geophys* 177:1193–1230. <https://doi.org/10.1007/s00024-019-02349-3>
- Rabinovich AB, Šepić J, Thomson RE (2020) The meteorological tsunami of 1 November 2010 in the southern Strait of Georgia: a case study. *Natural Hazards* (this issue)
- Salaree A, Mansouri R, Okal EA (2018) The intriguing tsunami of 19 March 2017 at Bandar Dayyer, Iran: field survey and simulations. *Nat Hazards* 90:1277–1307. <https://doi.org/10.1007/s11069-017-3119-5>
- Sallanger AH Jr, List JH, Gelfenbaum G, Stumpf RP, Hansen M (1995) Large wave at Daytona Beach, Florida, explained as a squall-line surge. *J Coast Res* 11:1383–1388
- Šepić J, Rabinovich AB (2014) Meteotsunami in the Great Lakes and on the Atlantic coast of the United States generated by the “derecho” of June 29–30, 2012. *Nat Hazards* 74:75–107. <https://doi.org/10.1007/s11069-014-1310-5>
- Šepić J, Vilibić I, Rabinovich AB, Monserat S (2015a) Widespread tsunami-like waves of 23–27 June in the Mediterranean and Black Seas generated by high-altitude atmospheric forcing. *Sci Rep* 5:11682. <https://doi.org/10.1038/srep11682>
- Šepić J, Vilibić I, Fine I (2015b) Northern Adriatic meteorological tsunamis: assessment of their potential through ocean modeling experiments. *J Geophys Res Oceans* 120:2993–3010. <https://doi.org/10.1002/2015JC010795>
- Šepić J, Vilibić I, Lafon A, Macheboeuf L, Ivanović Z (2015c) High-frequency sea level oscillations in the Mediterranean and their connection to synoptic patterns. *Prog Oceanogr* 137:284–298. <https://doi.org/10.1016/j.pocean.2015.07.005>
- Šepić J, Vilibić I, Rabinovich AB, Tinti S (2018a) Meteotsunami (“Marrobio”) of 25–26 June 2014 on the southwestern coast of Sicily, Italy. *Pure Appl Geophys* 175:1573–1593. <https://doi.org/10.1007/s00024-018-1827-8>
- Šepić J, Rabinovich AB, Sytov VN (2018b) Odessa tsunami of 27 June 2014: observations and numerical modelling. *Pure Appl Geophys* 175:1545–1572. <https://doi.org/10.1007/s00024-017-1729-1>
- Shi LM, Olabarrieta M, Nolan DS, Warner JC (2020) Tropical cyclone rainbands can trigger meteotsunamis. *Nat Commun* 11:678. <https://doi.org/10.1038/s41467-020-14423-9>
- Sibley A, Cox D, Long D, Tappin D, Horseburgh K (2016) Meteorologically generated tsunami-like waves in the North Sea on 1/2 July 2015 and 28 May 2008. *Weather* 71:68–74. <https://doi.org/10.1002/wea.2696>
- Soltanpour A, Pirooznia M, Aminjafari S, Zareian P (2018) Persian Gulf and Oman sea tide modeling using satellite altimetry and tide gauge data (TM-IR01). *Mar Georesour Geotech* 36(6):677–687. <https://doi.org/10.1080/1064119X.2017.1366608>
- Thoppil PG, Hogan PJ (2010) Persian Gulf response to a wintertime shamal wind event. *Deep Sea Res I* 57:946–955. <https://doi.org/10.1016/j.dsr.2010.03.002>
- Vennell R (2010) Resonance and trapping of topographic transient ocean waves generated by a moving atmospheric disturbance. *J Fluid Mech* 650:427–442. <https://doi.org/10.1017/S0022112009993739>
- Vilibić I (2008) Numerical simulations of the Proudman resonance. *Cont Shelf Res* 28:574–581. <https://doi.org/10.1016/j.csr.2007.11.005>



- Vilibić I, Domijan N, Orlić M, Leder N, Pasarić M (2004) Resonant coupling of a traveling air-pressure disturbance with the east Adriatic coastal waters. *J Geophys Res Oceans* 109:C10001. <https://doi.org/10.1029/2004JC002279>
- Vilibić I, Šepić J, Rangelov J, Strelec-Mahović N, Tinti S (2010) Possible atmospheric origin of the 7 May 2007 western Black Sea shelf tsunami event. *J Geophys Res* 115:C07006. <https://doi.org/10.1029/2009JC005904>
- Vilibić I, Horvath K, Strelec Mahović N, Monserrat S, Marcos M, Amores A, Fine I (2014) Atmospheric processes responsible for generation of the 2008 Boothbay meteotsunami. *Nat Hazards* 74:25–53. <https://doi.org/10.1007/s11069-013-0811-y>
- Vilibić I, Šepić J, Rabinovich AB, Monserrat S (2016) Modern approaches in meteotsunami research and early warning. *Front Mar Sci* 3:57. <https://doi.org/10.3389/fmars.2016.00057>
- Vučetić T, Vilibić I, Tinti S, Maramai A (2009) The Great Adriatic flood of 21 June 1978 revisited: an overview of the reports. *Phys Chem Earth* 34:894–903. <https://doi.org/10.1016/j.pce.2009.08.005>
- Wertman CA, Yablonsky RM, Shen Y, Merrill J, Kincaid CR, Pockalny RA (2015) Mesoscale convective system surface pressure anomalies responsible for meteotsunamis along the US East Coast on June 13th, 2013. *Sci Rep* 4:7143. <https://doi.org/10.1038/srep07143>
- Williams DA, Horsburgh KJ, Schultz DM, Hughes CW (2019) Examination of generation mechanisms for an English Channel meteotsunami: combining observations and modeling. *J Phys Oceanogr* 49:103–120. <https://doi.org/10.1175/JPO-D-18-0161.1>
- Williams DA, Horsburgh KJ, Schultz DM, Hughes CW (2020) Proudman resonance with tides, bathymetry and variable atmospheric forcings. *Nat Hazards*. <https://doi.org/10.1007/s11069-020-03896-y> (in press)

**Publisher's Note** Springer Nature remains neutral with regard to jurisdictional claims in published maps and institutional affiliations.

## Affiliations

Mohammad Hossein Kazeminezhad<sup>1</sup>  · Ivica Vilibić<sup>2</sup> · Cléa Denamiel<sup>2</sup> · Parvin Ghafarian<sup>1</sup> · Samaneh Negah<sup>3</sup>

✉ Mohammad Hossein Kazeminezhad  
mkazeminezhad@inio.ac.ir

<sup>1</sup> Iranian National Institute for Oceanography and Atmospheric Science, Etemad Zadeh St., Fatemi Ave., Tehran 14155-4781, Iran

<sup>2</sup> Institute of Oceanography and Fisheries, Šetalište I. Meštrovića 63, 21000 Split, Croatia

<sup>3</sup> I.R. Iran Meteorological Organization, Gilan Meteorology Office, Havashenasi St., Moallem Blv., Rasht, Gilan, Iran